Effect of magnetic field profile on the anode fall in a Hall-effect thruster discharge[a)]

L. Dorf,[b)] Y. Raitses, and N. J. Fisch
Princeton Plasma Physics Laboratory, Princeton, New Jersey 08543

(Received 24 October 2005; accepted 20 December 2005; published online 17 May 2006)

The effect of the magnetic field configuration on the anode fall in an $\vec{E}\times\vec{B}$ discharge of a Hall thruster is studied both experimentally and theoretically. Plasma potential, electron temperature, and plasma density in the near-anode region are measured with a biased probe in three configurations of the magnetic field. It is observed that the anode fall in a Hall thruster can be changed from negative to positive by creating a magnetic field configuration with a zero magnetic field region. Similar configurations are utilized in some advanced Hall thrusters, like an ATON thruster. Results of the measurements are employed to model a Hall thruster with different magnetic field configurations, including the one with a zero-field region. Different anode sheath regimes observed experimentally are used to set the boundary conditions for the quasineutral plasma. Numerical solutions obtained with a hydrodynamic quasi-one-dimensional model suggest that varying the magnetic field configuration affects the electron mobility both inside and outside the channel, as well as the plasma density distribution along the axis. © *2006 American Institute of Physics*.
[DOI: 10.1063/1.2174825]

I. INTRODUCTION

A plasma thruster with closed electron drift, or Hall thruster (HT), is currently one of the most advanced and efficient types of electrostatic propulsion devices.[1,2] The principle of operation of Hall thrusters is based on electrostatic acceleration of heavy ions in crossed electric and magnetic fields applied to a dc plasma discharge. Conventional Hall thrusters have a coaxial structure, and consist of electromagnetic coils with a ferromagnetic core, an anode that also serves as a gas distributor, a ceramic channel, and a cathode neutralizer (Fig. 1). The electric field is induced in a quasineutral plasma by an applied dc voltage V_d, typically of the order of several hundred volts. An applied radial magnetic field (with a maximum strength of typically between 100 and 200 G) in the presence of the axial electric field causes the magnetized electrons to drift in the azimuthal direction—this drift is called a Hall drift. The axial flow of electrons toward the anode is therefore impeded, providing sufficient electron residence time for effective ionization at a discharge current I_d, which does not greatly exceed a total outgoing ion current I_i. The ratio I_i/I_d is the definition of current utilization—one of the important factors determining thruster efficiency. Another advantage of employing a magnetic field in Hall thrusters is that, due to the decreased electron mobility, the main discharge voltage drop occurs in the plasma, and not in the non-neutral sheath near the cathode like in regular glow and arc discharges. Thus, the acceleration of unmagnetized ions by the electric field occurs in the quasineutral plasma, and is not limited by space-charge effects that are present, for example, in electrostatic-grid ion thrusters.[3–5] Experimental and theoretical studies of the effect of the radial magnetic field axial profile on Hall thruster operation concluded that plasma flow is more stable in regions where the magnetic field increases in the direction of ion flow, and more unstable (with respect to formation of an azimuthally rotating "spike" that perturbs uniformity of the discharge) in regions where magnetic field decreases.[6–8] Therefore, the magnetic field profile employed in conventional Hall thrusters generally satisfies the plasma flow stability criterion $dB_r(z)/dz>0$, along most of the thruster channel.

In a gas discharge, there can be either an increase or a drop in the plasma potential over a distance of a few Debye lengths from the anode, generally referred to in the literature as the "anode fall." When the anode is at a higher potential than the near-anode plasma, the anode fall is called "positive," and when it is at a lower potential—"negative." The positive and negative anode falls are associated with formation of the electron-attracting and electron-repelling anode sheaths, respectively. In spite of a number of experimental[9–20] and theoretical[21–25] studies of a Hall thruster internal plasma structure, the understanding of the anode sheath phenomena in Hall thrusters was, until recently, very limited. A more detailed review of previous works and additional motivation for studying the anode sheath phenomena in Hall thrusters can be found in Refs. 26 and 27. As was reported recently, a diagnostic apparatus comprising biased and emissive electrostatic probes, a high-precision positioning system, and low-noise electronic circuitry was developed and used for measurements in the near-anode region of a 12.3 cm Hall thruster operating in the 0.2–2 kW power range.[26,28] Accurate, nondisturbing measurements of the plasma potential allowed experimental identification of both electron-repelling (negative anode fall) and electron-

[a)]Paper RI2 7, Bull. Am. Phys. Soc. **50**, 310 (2005).
[b)]Invited speaker. Present address: Los Alamos National Laboratory, Los Alamos, NM 87545. Electronic mail: ldorf@lanl.gov

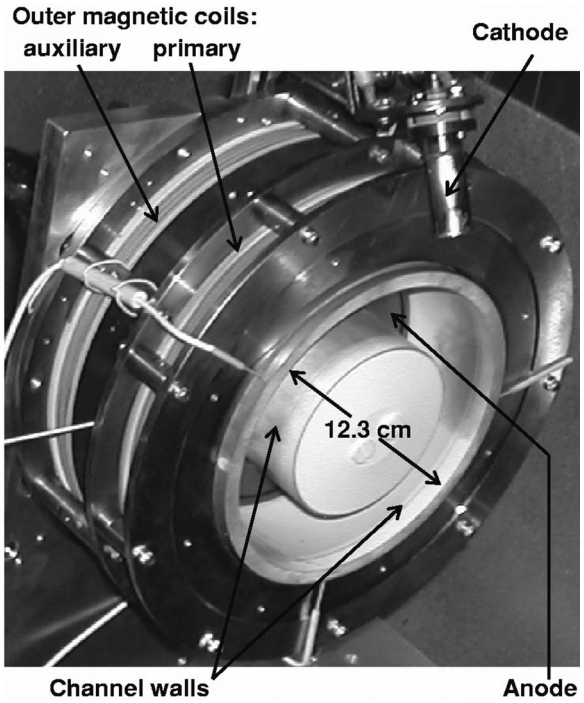

FIG. 1. The 2 kW laboratory Hall thruster with 12.3 cm outer channel wall diameter.

attracting (positive anode fall) anode sheaths in a HT. It was shown that at typical thruster operating conditions, the fall at the clean anode is negative, which is in agreement with the results of a recent theoretical study of the anode sheath in HTs.[26,27,29] At typical operating conditions, the thermal electron current to the anode, produced by ionization in the quasineutral plasma, is larger than the discharge current. Therefore, formation of a negative fall is required to repel the excessive electron flux from the anode.[26,27] Such anode fall behavior, essentially opposite to that in glow discharges, is the result of a very high ionization degree in HTs, achieved by applying a radial magnetic field transverse to the direction of the discharge current.

Similar to Hall thrusters, a magnetic field transverse to the direction of the discharge current is also utilized in other gas discharge devices, such as magnetrons, magneto-plasma-dynamic thrusters, and Hall-current ion sources. The effect of the magnetic field on anode and cathode falls in these devices and in regular dc-glow discharges was studied both experimentally and theoretically.[30–38] The use of the transverse magnetic field in glow discharges was generally shown to result in a decrease of the cathode potential drop and an increase of the anode potential drop, which was attributed to a reduced electron mobility.[32,33,35] Whereas in these works the magnetic field was typically homogeneous throughout the entire discharge, in conventional Hall thrusters the magnetic field is significant only in a so-called acceleration region, which starts about half of the channel length from the anode and where the main voltage drop occurs. Therefore, to study the effect of the magnetic field on the anode fall in Hall thrusters, a special magnetic field configuration with a nonzero field near the anode needs to be created.

In this paper we present results of plasma measurements

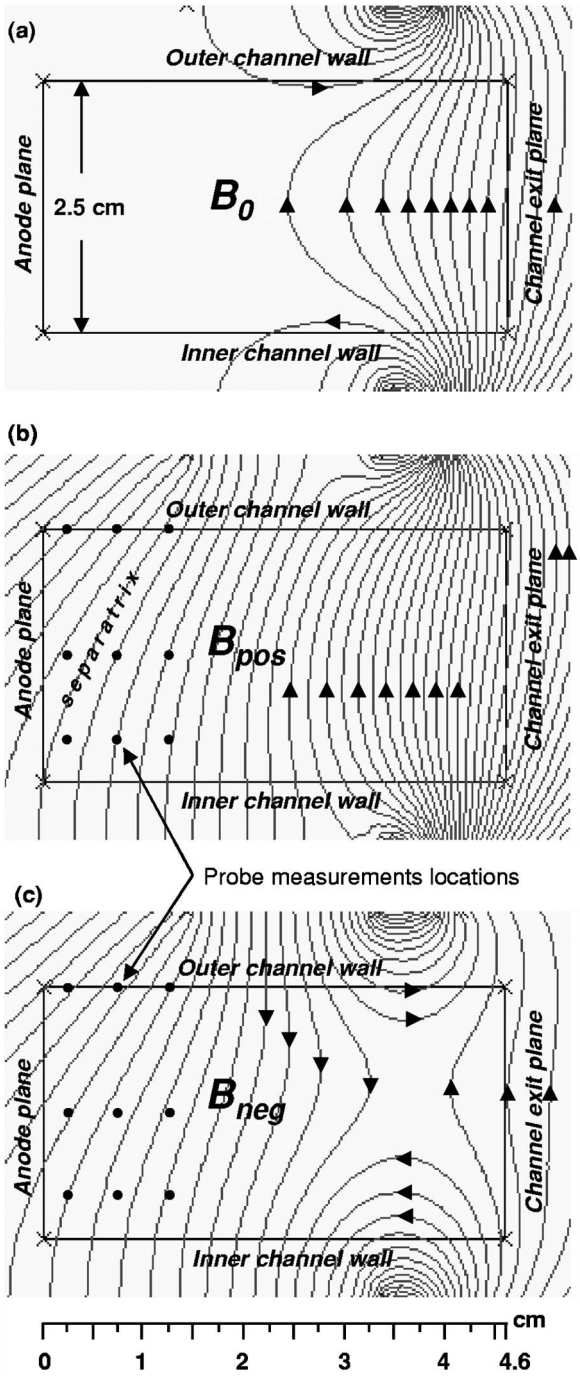

FIG. 2. Magnetic field lines in the 12.3 cm Hall thruster for three magnetic field configurations: B_0, B_{pos}, and B_{neg}. All diagrams are drawn to scale.

in the near-anode region of the 2 kW laboratory Hall thruster with three different configurations of the magnetic field, performed with a biased probe. A literature search suggests that there were no previous experimental studies of the effect of the magnetic field profile on the anode fall in Hall thrusters. The paper is organized as follows. In Sec. II, we describe the 12.3 cm Hall thruster with three different magnetic field configurations and the biased electrostatic probe apparatus used in this study. In Secs. III and IV, we discuss the results of plasma measurements, and examine the effect of the magnetic field on the anode fall. In Secs. V and VI, we introduce

the hydrodynamic quasi-one-dimensional (1D) model for a quasineutral plasma in a HT, and analyze the numerical solutions. We conclude in Sec. VII.

II. EXPERIMENTAL PROCEDURE

The test facility, the 2 kW laboratory Hall thruster, and the electrostatic probe apparatus used in this study are described in detail in Refs. 28 and 39. The thruster has a conventional annular configuration with a channel length $L_{ch}=46$ mm (which is in the 20–80 mm range typical for HTs),[9–20] a channel width $H_{ch}=25$ mm, and an outer channel wall diameter $D_{out}=12.3$ cm (Fig. 1). In the present experiments, the thruster was operated at xenon gas mass flow rate $\dot{m}=3$ mg/s, and at the discharge voltage $V_d=300$ V. The anode surface facing the plasma was thoroughly cleaned before the experiments to ensure its conductivity.[26]

The magnetic field in the thruster was created by one inner and two outer, primary and auxiliary, electromagnetic coils (Fig. 1). The currents in the inner and primary outer coils were kept equal to 1.3 A throughout the experiments, whereas different currents ($I_c=0$, $I_c=1.4$ A, and $I_c=-1.4$ A), were supplied to the auxiliary outer coil to create three configurations of the magnetic field: B_0, B_{pos}, and B_{neg}, respectively. Figure 2 shows results of nonlinear simulations of the magnetic field distribution. Simulations were conducted using measured B-H curve of the low carbon steel used in the thruster design. A comparison of simulated and measured results showed a very good agreement.

The plasma potential, plasma density, and electron temperature were measured at 2, 7, and 12 mm from the anode with a movable biased electrostatic probe of planar geometry. The probe was introduced radially into the near-anode region through the axial slot made in the outer channel wall. As was reported in Ref. 28, the motion of the radially oriented probe near the anode does not cause perturbations to the Hall thruster discharge. The plasma measurements were performed at several distances from the thruster axis: at the outer wall (OW), $R=62$ mm, at the midpoint between the channel walls (MC), $R=49$ mm, and near the inner wall (IW), $R=41$ mm, as shown in Fig. 2.

The biased planar probe was constructed of 0.76 mm diameter thoriated tungsten rod, covered by a high purity alumina single-bore tube with outer diameter of 1.3 mm and inner diameter of 0.79 mm. For the unmagnetized probe theory to be valid for a cylindrical probe introduced into plasma perpendicular to the magnetic field lines, the probe diameter must be much smaller than the electron gyrodiameter.[40] A similar criterion for a planar probe introduced into plasma at an angle to the magnetic field can be formulated as that the collecting rod diameter d, projected onto the magnetic field line must be much smaller than the electron gyrodiameter. When the planar probe is introduced radially into the thruster channel, this criterion can be expressed as $d \ll 4.8\sqrt{T_e[\mathrm{eV}]}/B_z\,[\mathrm{G}]$, where B_z is the axial component of the magnetic field. In this study, the most severe limitation is imposed in B_{neg} configuration for measurements at the outer wall and at 7 mm from the anode: $d_{pr} \ll 2$ mm. For the collecting rod diameter employed ($d=0.76$ mm), this limitation is marginally satisfied.

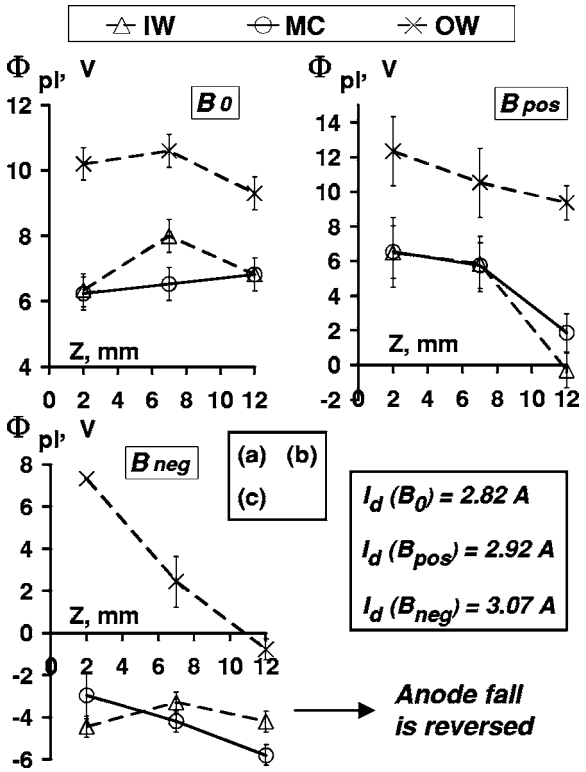

FIG. 3. Plasma potential axial profiles $\Phi_{pl}(z)$ for three magnetic field configurations (B_0, B_{pos}, and B_{neg}) measured with the biased probe at several radial locations—at the outer wall (OW), at the midpoint point between channel walls (MC), and at 4 mm from the inner wall (IW)—in the near-anode region of the 12.3 cm Hall thruster at $V_d=300$ V and $\dot{m}=3$ mg/s. $Z=0$ is chosen at the anode, and Φ_{pl} is shown relative to the anode potential. Also shown are measured discharge currents I_d.

III. EXPERIMENTAL RESULTS

Figure 3 shows plasma potential axial profiles $\Phi_{pl}(z)$, measured in the near-anode region of the 12.3 cm Hall thruster with three magnetic field configurations—B_0, B_{pos}, and B_{neg}—along with the measured discharge current I_d. At each of the nine locations inside the channel, measurements were performed sequentially in all three configurations of the magnetic field. The error bars for Φ_{pl} measured at the outer wall and at 2 mm from the anode in B_{neg} configuration are not shown in the Fig. 3(c). A kink in the probe current-voltage characteristic (I_{PR} versus V_{PR}), normally used to determine plasma potential,[28] was hard to distinguish for this data point due to the lack of plasma at the described location inside the channel. Instead, the kink in the $\ln(I_{PR})$ versus V_{PR} plot was used, and the uncertainty in determining Φ_{pl} by this method is hard to estimate.

As can be seen from Fig. 3(a), the plasma potential at 2 mm from the anode is higher than the anode potential in all three radial locations (IW, MC, and OW), which indicates the presence of a negative anode fall, or electron-repelling anode sheath, in a conventional Hall thruster with the B_0 configuration of the magnetic field. In the quasineutral plasma between the anode and the acceleration region, the

electron drift velocity, $V_{\mathrm{dr}} \sim I_d/(eN_0AA) \approx 6\times 10^6$ cm/s, is much smaller than the average velocity of the half-Maxwellian electron flux traveling towards the anode, $V_{\mathrm{HM}} = \sqrt{2T_e/(\pi m_e)} \approx 8\times 10^7$ cm/s, as can be estimated using the channel cross section $AA = 77$ cm^2, the measured discharged current $I_d = 2.82$ A, and the plasma density N_0, along with the electron temperature T_e, measured at the midpoint between the channel walls at 2 mm from the anode [Figs. 4(a) and 4(d)]. At the mass flow rates typical for the HTs, electron-neutral collisions are very weak near the anode ($\Lambda_{en} \sim \Lambda_{nn} \approx 10-20$ cm), and so is the magnetic field in the conventional HT configuration [Fig. 2(a)]. Therefore, to create a reversed electron flux and reduce the net electron velocity, formation of the electron-repelling anode sheath is required in B_0 configuration.

In B_{pos} and B_{neg} configurations, most of the plasma in the near-anode region is concentrated between the inner wall and the channel median, as follows from measurements of the plasma density axial profiles $N(z)$, at three radial locations: IW, MC, and OW [Figs. 4(b) and 4(c)]. Furthermore, the plasma density near the inner wall and near the channel median at 2 mm from the anode is almost the same in these configurations as it is in B_0 configuration, in which the near-anode magnetic field is negligible [Fig. 2(a)]. Interestingly, measurements at 2.5 mm from the anode in a discharge similar to the Hall thruster discharge showed that the near-anode plasma density increases with the increase of the magnetic field.[30] However, in Ref. 30, the magnetic field was uniform throughout the entire discharge, and it was strictly parallel to the anode surface, unlike the near-anode magnetic field in B_{neg} and B_{pos} configurations in the present study [Figs. 2(b) and 2(c)].

In B_{pos} and B_{neg} configurations, the radial magnetic field in the near-anode region is comparable to that in the acceleration region (Fig. 2). The radial magnetic field impedes the electron motion toward the anode. In B_{pos} configuration, the electron transport across the magnetic field is provided by the negative axial gradient of the plasma potential and the positive axial gradient of the electron pressure, observed at the IW and MC radial locations [Figs. 3(b) and 4(b)]. In the B_{neg} configuration, the electron transport across the magnetic field is governed mainly by the axial electron pressure gradient, $(1/eN)(dP/dz) \sim 8$ V/cm, since it is larger than the gradient of the plasma potential near the inner wall and at the channel median [Figs. 3(c) and 4(c)]. In the near-anode region, the ion velocity is much less than the electron velocity and the electron temperature is almost constant along the channel [Figs. 4(e) and 4(f)]. Therefore, at 7–12 mm from the anode in B_{pos} and B_{neg} configurations, the phenomenological electron momentum equation describing the electron axial transport across the magnetic field[29] can be written as $J_d \approx \mu_e[(T_e/e)dN/dz - Nd\Phi_{\mathrm{pl}}/dz]$, where $J_d = I_d/(eAA)$, e is the absolute value of the electron charge, and μ_e is the electron axial mobility in a radial magnetic field. Using the measured plasma potential, plasma density, and electron temperature (Figs. 3 and 4), and assuming that at 7–12 mm from the anode, N and Φ_{pl} are linear functions of z, the value of the electron axial mobility in the near-anode region in B_{pos} and B_{neg} configurations can be estimated as

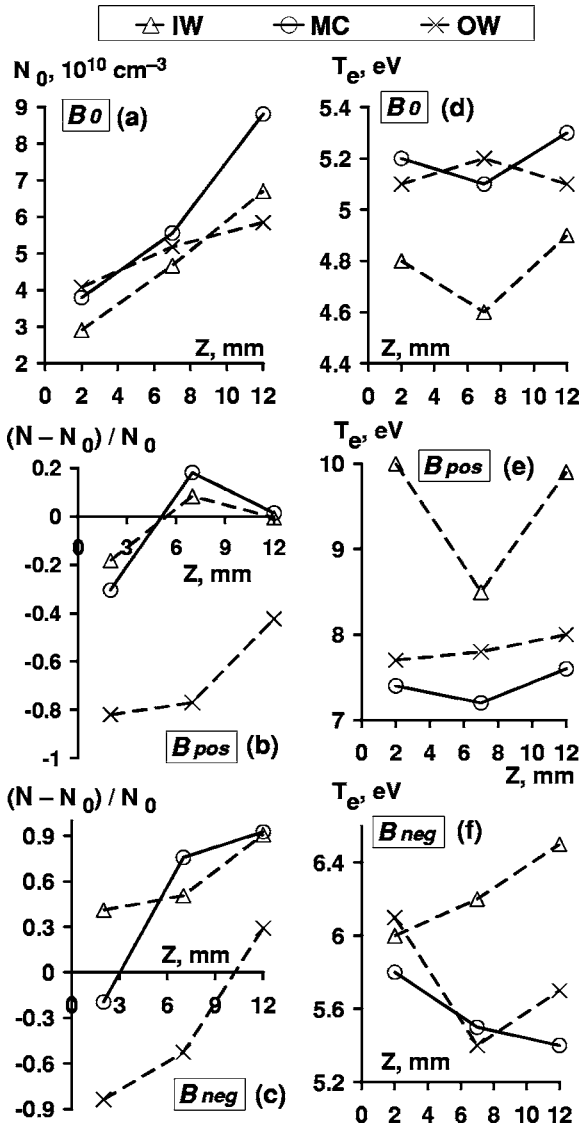

FIG. 4. (a) Plasma density axial profiles $N_0(z)$ for B_0 configuration. (b) and (c) Relative density profiles, $[N(z)-N_0(z)]/N_0(z)$, for B_{pos} and B_{neg} configurations. (d)–(f) Electron temperature profiles $T_e(z)$ for all three configurations. Measured with the biased probe at several radial locations—at the outer wall (OW), at the midpoint between channel walls (MC), and at 4 mm from the inner wall (IW)—in the near-anode region of the 12.3 cm Hall thruster at the discharge voltage $V_d = 300$ V and the mass flow rate $\dot{m} = 3$ mg/s. Z=0 is chosen at the anode.

$\mu_e \sim (1/7-1/4)|B_r|^{-1} \sim (20-30)$ T^{-1}, which is greater that the Bohm value $\mu_e = (1/16)|B_r|^{-1}$. Note that for the low-power cylindrical Hall thruster (CHT), which has a cusp magnetic field configuration similar to B_{neg}, the value of the electron axial mobility that gives the best agreement between the simulations and experiments was found to be close to the Bohm value.[41] The same is true for the value of the electron mobility obtained experimentally in Hall thrusters,[19] whereas the value of the axial mobility typically used in theoretical models is significantly smaller than the Bohm value.[21,29,42]

Note also that the anomalous electron transport in HTs is believed to be induced by high-frequency plasma instabilities. Interestingly, in the frequency range below ~100 kHz, the 2.6 cm CHT with the cusp magnetic field operates more quietly than the annular Hall thruster of the same size.[43] The

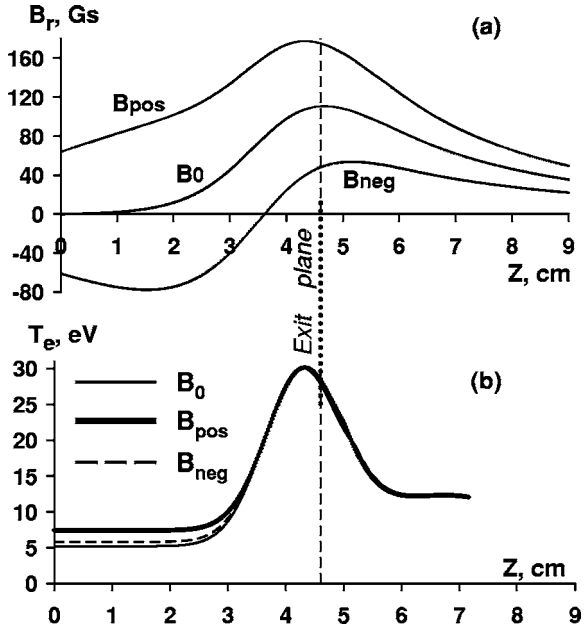

FIG. 5. (a) Radial magnetic field axial profiles in the 12.3 cm Hall thruster for three magnetic field configurations: B_0, B_{pos}, and B_{neg}. Simulated along the midline between the channel walls, using the *B-H* curve for the carbon steel employed in the magnetic system design. (b) Temperature profiles used in numerical modeling with the three configurations of the magnetic field. $Z=0$ lies in the anode plane.

theoretical study of a HT, reported in Ref. 44, also shows that the amplitude of the low-frequency current oscillations (10–20 kHz) decreases, when the *B* field configuration exhibits a zero field inside the channel. This improved stability has been observed experimentally in the ATON Hall thruster, where the magnetic field topology includes a point of zero-*B* field.[44–46] Finally, in Ref. 47, the stabilization of a longitudinal dc discharge is achieved by applying a spatially periodic radial external magnetic field that varies in sign along the axis of the coaxial system. The uniformity of the discharge improves because of the presence of a sheer plasma flow with periodically changing azimuthal velocity, created by the periodic $\vec{J}\times\vec{B}$ force. In summary, transport-inducing instabilities might be reduced in a HT by the presence of the zero magnetic field region. In light of the above, one intuitively appealing argument is that the reversal of polarity of the anode fall in B_{neg} configuration [Fig. 3(c)] could be attributed to the reduced mobility inside the channel.

IV. ANODE FALL IN B_{pos} AND B_{neg} CONFIGURATIONS

As can be seen from Figs. 2(b) and 2(c), electrons that are transferred sufficiently close to the anode can reach the anode along the magnetic field lines. In Fig. 2(b), the magnetic field line that separates the electrons bouncing between the channel walls from the electrons escaping to the anode is labeled "separatrix." Electron thermal motion toward the anode along the magnetic field lines is not impeded by the magnetic field. Moreover, bulk of the electrons transferred onto the magnetic field lines connected to the anode with longitudinal velocities directed toward the outer wall are repelled by the wall sheath, and eventually also reach the anode (Fig. 2). Therefore, it can be assumed that in B_{pos} and B_{neg} configurations, the potential drop between the near-anode plasma and the anode is again required to repel the excessive electron flux from the anode. This could explain the presence of the negative anode fall observed at IW and MC radial locations in the B_{pos} configuration of the magnetic field [Fig. 3(b)]. The structure of this sheath is not significantly affected by the magnetic field, because near the anode, the Larmor radius, $\rho_L=2.4\sqrt{T_e\ [\mathrm{eV}]}/B\ [\mathrm{G}]\sim 0.8$ mm, is 6–8 times greater than the Debye length, as can be estimated using the electron temperature and the plasma density measured at 2 mm from the anode near the inner wall and at the midpoint between the channel walls.

The following estimation can illustrate the physical picture described above. Assume: (a) that at 2 mm from the anode, only electrons repelled by the voltage drop in the anode sheath (Φ_{pl}) have longitudinal velocities directed toward the outer wall; and (b) that velocity distribution for electrons with longitudinal velocities directed toward the anode is half-Maxwellian. In this case, the total electron current toward the anode through the plane crossing the channel at 2 mm from the anode can be estimated as

$$I_e = eNV_{\parallel}^e \cos\alpha\, A_{\mathrm{eff}}, \tag{1}$$

where

$$V_{\parallel}^e = \sqrt{(2/\pi)T_e/m_e}\,\exp(-e\Phi_{pl}/T_e)/[1+\mathrm{erf}(\sqrt{e\Phi_{pl}/T_e})] \tag{2}$$

and

$$A_{\mathrm{eff}} = \beta AA. \tag{3}$$

In Eqs. (1) and (2), all plasma properties are obtained by averaging between the values measured at IW and MC radial locations at 2 mm from the anode; $\alpha\approx 60°$ is the angle between the magnetic field lines and the thruster axis; and (βAA) is the effective cross-sectional area of the channel, which takes into account that not all magnetic field lines in the considered cross section intersect with the anode [Figs. 2(b) and 2(c)], and that the plasma density measured at the outer wall is much smaller than that measured at the midpoint between the walls or near the inner wall. Using the plasma potential, plasma density, and electron temperature measured in B_{pos} configuration at 2 mm from the anode [Figs. 3(b), 4(b), and 4(e)], the electron current toward the anode in this magnetic configuration can be evaluated as $I_e \approx \beta_{pos}\,4.5$ A. Considering that at 2 mm from the anode the ion current constitutes a negligible part of the discharge current ($I_d=2.92$ A), the numerical factor β in B_{pos} configuration can be then estimated as

$$\beta_{pos} \approx I_d/4.5 \approx 0.65. \tag{4}$$

In B_{neg} configuration, the plasma potential measured at 2 mm from the anode near the inner wall and at the channel median is lower than the anode potential [Fig. 3(c)], which indicates the presence of a positive anode fall. Electrons traveling toward anode along the magnetic field lines are therefore not repelled by the voltage drop between the anode and the near-anode plasma. Using Eq. (1) with $\Phi_{pl}=0$ and plasma density *N*, measured in the B_{neg} configuration at 2 mm from the anode [Fig. 4(c)], it can be obtained that

$$I_e = \beta_{\text{neg}} \sqrt{T_{\parallel}\,[\text{eV}]} 6.25\ \text{A}, \tag{5}$$

where $T_{\parallel}$ is the temperature associated with the electron motion along magnetic field lines. Assuming that $\beta_{\text{neg}} = \beta_{\text{pos}} = 0.65$, and using the value of the discharge current measured in the B_{neg} configuration ($I_d = 3.07$ A) it can be obtained that the parallel temperature should be equal to $T_{\parallel} \approx 0.6$ eV. The electron temperature measured in the B_{neg} configuration at all three radial locations at 2 mm from the anode is about 6 eV [Fig. 4(f)]. The electron temperature measured by a planar probe in the bi-Maxwellian plasma in the magnetic field is $T_e = T_{\parallel} \sin^2 \alpha + T_{\perp} \cos^2 \alpha$, where $T_{\perp}$ is the temperature associated with electron Larmor gyration, and α is the angle between the magnetic field and the collecting plane of the probe (for a radially inserted probe, α is the same as the angle between the magnetic field and the thruster axis). Thus, for $T_{\parallel} \approx 0.6$ eV, it can be obtained that $T_{\perp} \approx 24\ \text{eV} \approx 40 T_{\parallel}$. Physical mechanisms that could account for such strong anisotropy in the near-anode electron temperature are not apparent. Alternatively, it could be assumed that in the B_{neg} configuration, the numerical factor β is different from that in the B_{pos} configuration. For the isotropic electron temperature, $T_{\parallel} = T_{\perp} = T_e = 6$ eV, it can be obtained that in the B_{neg} configuration

$$\beta_{\text{neg}} = 0.2, \tag{6}$$

which is about three times less than that in the B_{pos} configuration. Deeper understanding of such intricate phenomenon as the presence of a positive anode fall in the B_{neg} configuration has yet to be obtained.

V. THEORETICAL MODEL

General issues associated with modeling of Hall thrusters are described in detail in Refs. 24 and 29. In this section, the quasi-1D model with a given temperature profile introduced in Ref. 24, along with the results of measurements in the near-anode region presented in Sec. III, are employed to describe the behavior of the quasineutral plasma in the 12.3 cm Hall thruster with three different configurations of magnetic field (Fig. 2).

Using the experimentally obtained discharge current and near-anode plasma density along with a given temperature profile allows theoretical evaluation of certain plasma properties, like the electron axial mobility, which are hard to characterize experimentally. In contrast to Ref. 29, nonquasineutral plasma in the anode sheath is not considered here; instead, different anode sheath regimes observed experimentally are used to set the boundary conditions (BC) for the quasineutral plasma. Consequently, the voltage drop in the anode sheath is neglected, and the entire discharge voltage $V_d = 300$ V, is applied here to the quasineutral plasma. To make use of the experimental results, the propellant (xenon) mass flow rate of $\dot{m} = 3$ mg/s and the radial magnetic field axial profiles given in Fig. 5(a) are used in numerical simulations. These magnetic field profiles are simulated along the midline between the channel walls, using the *B-H* curve for the carbon steel employed in the magnetic system design.

Incorporating the electron energy balance equation into the full system of equations proved to be a rather difficult task in conventional HTs, due in part to a non-Maxwellian shape of the electron distribution function, which was observed in HTs.[48,49] In a HT with a nonconventional magnetic field configuration this task becomes even more complicated, due to the presence of a significant axial component of the magnetic field. The axial magnetic field impedes electron motion toward the channel walls, which could reduce the electron energy losses in that region. For the above reasons and due to the lack of the experimentally obtained temperature profiles in the B_{pos} and B_{neg} configurations, the same temperature profile (corrected for the measured values of the near-anode temperature) was used here in modeling with all three configurations of the magnetic field [Fig. 5(b)]. This temperature profile was measured with the fast reciprocating emissive probe[39] in the same 12.3 cm HT with conventional magnetic field configuration, at $V_d = 300$ V, $\dot{m} = 3$ mg/s, and currents in the inner and primary outer coils equal to 1 and 2.5 A, respectively.

This measured profile is also used in modeling outside the channel, thus eliminating the need for a specific BC for electron temperature in the exit plane. In general, outside the channel, we use the same 1D description as inside, with the exception that the wall losses are considered to be zero. As will be seen from Sec. V, the computation is only continued to about 1.7 cm past the physical location of the cathode ($Z_{\text{cath}} = 5.4$ cm). This point lies on the magnetic field line that crosses the actual cathode-neutralizer. Therefore, the two-dimensional (2D) effects associated with the plume divergence, and the fact that the total current is zero in the far-plume, are not expected to change the main conclusions of this work.

We use here the same system of fluid equations as in Refs. 24 and 29:

$$J_i' = \langle \sigma V \rangle n_a n - 0.55 n \sqrt{(T_e/M_i)} (2/H_{\text{ch}}) \tag{7}$$

is the ion continuity equation. Here, the prime sign denotes the derivative with respect to z, $J_i = nV_i$ is the ion flux, n is the plasma density, V_i is the ion flow velocity, M_i is the xenon ion mass, and n_a is the neutral density.

$$(J_i V_i)' = eEn/M_i - 0.55 n \sqrt{(T_e/M_i)} (2/H_{\text{ch}}) V_i + \langle \sigma V \rangle n_a n V_a \tag{8}$$

is the ion momentum equation. Here, E is the axial projection of the electric field, and V_a is the neutral flow velocity, respectively.

$$n_a V_{a0} + J_i = J_m \tag{9}$$

represents mass conservation. Here, $J_m = \dot{m}/(M_i AA)$ is the propellant flux.

$$-en\mu_e^{-1} V_e = eEn + (nT_e)' \tag{10}$$

is the phenomenological electron momentum equation, in which μ_e is the absolute value of the electron axial mobility in a radial magnetic field. We assume a modified Bohm diffusion with $\mu_e = \alpha/[16|B_r(z)|]$, where the fitting parameter α is to be determined by the modeling.

$$-nV_e + J_i = J_d \tag{11}$$

represents charge conservation. Here, $J_d = I_d/(eAA)$, and the measured values of the discharge current I_d, given in Fig. 3, were used for modeling in each configuration of the magnetic field.

The system of equations (7)–(11) can be reduced to the system of two ordinary differential equations for the plasma density $n(z)$, and the ion flux $J_i(z) = n(z)V_i(z)$, of the form

$$\begin{cases} dJ_i/dz = F(J_i, n, J_d, \alpha) \\ dn/dz = G(J_i, n, J_d, \alpha)/(1 - V_i^2/V_s^2) \end{cases}, \tag{12}$$

where F and G are nonlinear functions, and $V_s = \sqrt{T_e/M_i}$ is the ion acoustic velocity. In all three configurations of the magnetic field, a solution of the system (12) can be constructed, if the ion velocity and the plasma density at the anode (V_{i0} and n_0, respectively) and the electron mobility coefficient (α) are specified. The plasma density measured at 2 mm from the anode at the midpoint between the channel walls [Figs. 4(a)–4(c)] is used in this modeling as n_0. Based on observations of the electron-repelling anode sheath in B_0 and B_{pos} configurations [Figs. 3(a) and 3(b)], a back ion flow with the ion acoustic velocity at the quasineutral plasma boundary is assumed in these configurations to set the boundary condition for the ion velocity: $V_{i0} = -V_s$. In B_{neg} configuration, a zero ion velocity is assumed at $z=0$; i.e., $V_{i0}=0$. Finally, similarly to Ref. 24, it can be shown that for each pair of V_{i0} and n_0, there is only one value of α for which a solution is regular at the sonic transition point, $V_i = V_s$.

VI. NUMERICAL RESULTS

System (12) was integrated numerically in all three configurations of the magnetic field: B_0, B_{pos}, and B_{neg}. The integration was initiated at the anode ($z=0$) and terminated at the point in the cathode plane ($z=L_{\text{cath}}$), determined by

$$\int_0^{L_{\text{cath}}} E(z)dz = V_d. \tag{13}$$

In the B_0 configuration, the cathode plane was found to be at 7.16 cm from the anode. As follows from the emissive probe measurements performed in the same 12.3 cm HT,[39] the plasma potential almost does not change with z for $z - z_{\text{exit}} \geqslant 2$ cm, or $z \geqslant 6.6$ cm. Thus, the position of the cathode plane found for the B_0 configuration is in a reasonable agreement with experiment. For the B_{neg} and B_{pos} configurations, however, it was impossible to select a realistic L_{cath} based on Eq. (13), because even for $z=10$ cm, the electric potential was found to be only about 110 and 180 V below the anode potential, respectively, whereas the discharge voltage is $V_d=300$ V. Furthermore, for $z \geqslant 30$ cm, the potential saturated at approximately 150 and 240 V, respectively, below the anode potential. To satisfy Eq. (13), the electron mobility coefficient α outside the channel was allowed to be different from that inside the channel; and L_{cath} was selected the same as that in B_0 configuration. Note also that in Ref. 39, the voltage drop measured between the anode and the cathode plane was actually found to be less than V_d by up to 50–70 V, depending on the mass flow rate and V_d. This could mean that Eq. (13) needs to be changed to reflect the actual voltage drop. We showed numerically that if $V_d=250$ V is considered with the rest of BC unchanged, this slightly changes the cathode plane location in the B_0 configuration, and has no effect on the main conclusions of this work.

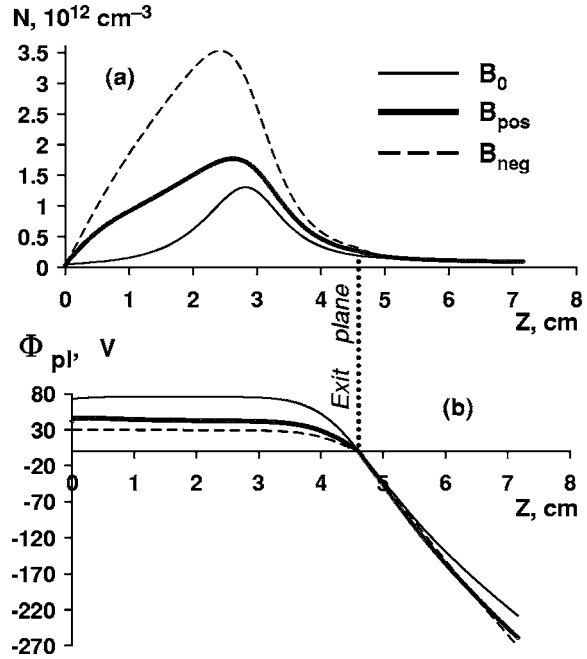

FIG. 6. Numerically obtained (a) plasma density $N(z)$ and (b) plasma potential profiles in the 12.3 cm Hall thruster with three magnetic field configurations: B_0, B_{pos}, and B_{neg}. $V_d=300$ V and $\dot{m}=3$ mg/s. All solutions are constructed on the interval between the anode and the cathode planes: $Z=0$ and $Z=L_{\text{cath}}=7.16$ cm, respectively. Zero potential is chosen at the channel exit: $Z=4.6$ cm.

The plasma density and plasma potential obtained numerically in all three configurations of the magnetic field are given in Fig. 6. As can be seen from Fig. 6(a), the peak plasma density obtained in the B_{neg} configuration is significantly larger than it is in the B_0 and B_{pos} configurations. This behavior cannot be attributed to the fact that in the B_0 and B_{pos} configurations, a different boundary condition for the ion velocity was used at $z=0$, as it was shown numerically that changing the boundary condition to $V_{i0}=0$ does not significantly affect the peak density in these configurations. The following analysis can explain why the numerically obtained peak density in the B_{neg} configuration is higher than that in the B_{pos} configuration (a similar analysis can be used for comparison between the B_{neg} and B_0 configurations). Using Eqs. (7)–(11), it can be obtained that

$$N_{\max} \approx (J_d - J_i)/(\mu_e T_e' e) - J_i/(T_e'/M_i) \times \{2\langle \sigma V_e \rangle (J_m - J_i)/V_a - 1.1 V_s/H_{ch}\}, \tag{14}$$

where $N_{\max} = N(z_{\max})$ is the peak density, and all functions on the right-hand side (RHS) of Eq. (14) are evaluated at $z=z_{\max}$. In both configurations, the location of the maximum is almost the same ($z_{\max} \sim 2.5$ cm), as well as T_e' at this point. However, the first term on the RHS of Eq. (14) is greater in

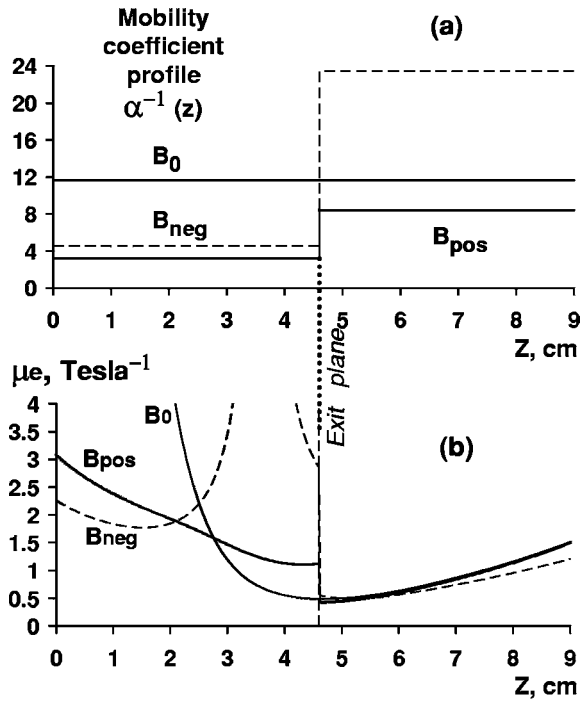

FIG. 7. Axial profiles of (a) the reversed electron mobility coefficient $\alpha^{-1}(z)$, and (b) the electron axial mobility $\mu_e(z)$, obtained numerically for the 12.3 cm Hall thruster with three magnetic field configurations: B_0, B_{pos}, and B_{neg}. Discharge voltage V_d=300 V and mass flow rate $\dot{m}$=3 mg/s. Z =0 lies in the anode plane.

the B_{neg} configuration, whereas the second term is greater in the B_{pos} configuration. The above is due to the fact that the ion flux at $z=z_{\max}$, i.e., $J_i(z_{\max})$, is greater in the B_{pos} configuration than it is in the B_{neg} configuration, which, in turn, is due to the larger near-anode electron temperature in B_{pos} configuration.

The reversed electron mobility coefficients α^{-1} obtained numerically in all three configurations of the magnetic field are given in Fig. 7(a). These coefficients were used to plot the axial electron mobility profiles $\mu_e(z)$ given in Fig. 7(b). Inside the channel, the largest α is found in B_{pos} configuration, and the smallest α is found in B_0 configuration. The numerical solutions obtained in the B_{neg} and B_{pos} configurations suggest that the electron mobility coefficient outside the thruster channel is several times smaller than it is inside, and that the most part of the discharge voltage drop occurs outside the channel, where the electron mobility is generally smaller. In the stationary plasma thruster model reported in Ref. 50, different mechanisms of the electron mobility and different mobility coefficients were considered inside and outside the thruster channel. In this model, most of the discharge voltage drop was also found to be in the region with smaller electron mobility.

VII. SUMMARY AND CONCLUSIONS

The effect of the magnetic field profile on the anode fall in a 2 kW laboratory Hall thruster is studied both experimentally and theoretically. Plasma potential, electron temperature, and plasma density in the near-anode region are measured with a biased probe in three configurations of the magnetic field. In varying the magnetic field topology in the channel from a more uniform to a cusp-like one with a zero-field region, we uncover intriguing results. For cusp configurations, in which the radial magnetic field changes polarity somewhere along the channel, the anode fall is positive, whereas it is negative for a more uniform field. This polarity difference could be attributed to the decreased electron mobility across the magnetic field in the cusp-like configuration. Most interesting is that it is the magnetic field topology in the bulk of the discharge, far from the anode, which determines the sign of the anode fall. This new information about the anode sheath in different configurations of the magnetic field now can underpin theoretical modeling in a variety of applications by setting proper boundary conditions at the anode. Different anode sheath regimes observed experimentally were used here to set the boundary conditions for the quasineutral plasma. Numerical solutions obtained with a hydrodynamic quasi-1D model suggest that varying the magnetic configuration affects the electron mobility both inside and outside the channel, as well as the plasma density distribution along the axis. Namely, it was found that in the cusp configuration with a zero-field region: (1) the electron mobility outside the channel must be assumed to be several times smaller than the mobility inside to allow the voltage drop over the discharge be equal to the applied voltage, and (2) the peak plasma density is several times as big as the peak density in the other two configurations studied. Different mobilities inside and outside the channel have been discussed in recent theoretical works in conjunction with modeling of the conventional (like SPT-100) and advanced (like ATON) thrusters. In these models, like in our work, the most part of the discharge voltage drop was also found to be in the region with smaller electron mobility. We would like to conclude with noting that in the cusp-like configuration used in this work, the complicated 2D structure of the magnetic field lines might change the actual wall losses inside the channel, thus affecting ionization and therefore density and potential distributions.[51] It may also cause anisotropy in the electron velocity distribution function. Considering these issues, however, lies out of the scope of this paper.

ACKNOWLEDGMENTS

The authors wish to thank A. Smirnov for fruitful discussions.

This work was supported by the US DOE under Contract No. DE-AC02-76CH03073.

[1] A. I. Morozov and V. V. Savelyev, in *Reviews of Plasma Physics*, edited by B. B. Kadomtsev and V. D. Shafranov (Kluwer Academic/Plenum, New York, 2000), Vol. 21.
[2] V. V. Zhurin, H. R. Kaufman, and R. S. Robinson, Plasma Sources Sci. Technol. **8**, R1 (1999).
[3] R. G. Jahn, *Physics of Electric Propulsion* (McGraw-Hill, New York, 1968).
[4] H. R. Kaufman, J. Spacecr. Rockets **9**, 511 (1972).
[5] R. G. Jahn and E. Y. Choueiri, in *Encyclopedia of Physical Science and Technology*, 3rd ed. (Academic, San Diego, 2002), Vol. 5, p. 125.
[6] A. I. Morozov, Yu. V. Esipchuk, A. M. Kapulkin, V. A. Nevrovskii, and V. A. Smirnov, Sov. Phys. Tech. Phys. **17**, 482 (1972).

[7] A. I. Morozov, in *Plasma Accelerators* (a collection of papers from the 1st All-Union Conference on Plasma Accelerators), edited by L. A. Artsimovich, S. D. Grishin, G. L. Grodzovsky, L. V. Leskov, A. I. Morozov, A. A. Porotnikov, A. M. Dorodnov, V. G. Padalka, and M. I. Pergament (Mashinostroenie, Moscow, 1973), p. 85 [Russian].
[8] A. I. Morozov and V. V. Savelyev, in *Reviews of Plasma Physics*, edited by B. B. Kadomtsev and V. D. Shafranov (Kluwer Academic/Plenum, New York, 2000), Vol. 21, p. 351.
[9] A. I. Morozov, Yu. V. Esinchuk, G. N. Tilinin, A. V. Trofimov, Yu. A. Sharov, and G. Ya. Shchepkin, Sov. Phys. Tech. Phys. **17**, 38 (1972).
[10] I. V. Melikov, Sov. Phys. Tech. Phys. **19**, 35 (1974).
[11] I. V. Melikov, Sov. Phys. Tech. Phys. **22**, 452 (1977).
[12] A. M. Bishaev and V. Kim, Sov. Phys. Tech. Phys. **23**, 1055 (1978).
[13] G. Guerrini, C. Michaut, M. Bacal, A. N. Vesselovzorov, and A. A. Pogorelov, Rev. Sci. Instrum. **69**, 804 (1998); see also: G. Guerrini, C. Michaut, M. Dudeck, A. N. Vesselovzorov, and M. Bacal, in *Proceedings, 25th International Electric Propulsion Conference*, Cleveland, 1997 (Electric Rocket Propulsion Society, Cleveland, OH, 1997), IEPC Paper 1997-053.
[14] Y. Raitses, J. Ashkenazy, and M. Guelman, J. Propul. Power **14**, 247 (1998).
[15] Y. Raitses, L. A. Dorf, A. A. Litvak, and N. J. Fisch, J. Appl. Phys. **88**, 1263 (2000).
[16] N. J. Fisch, Y. Raitses, L. A. Dorf, and A. A. Litvak, J. Appl. Phys. **89**, 2040 (2001).
[17] Y. Raitses, M. Keidar, D. Staack, and N. J. Fisch, J. Appl. Phys. **92**, 4906 (2002).
[18] J. M. Haas and A. D. Gallimore, Phys. Plasmas **8**, 652 (2001).
[19] N. B. Meezan, W. A. Hargus, Jr., and M. A. Cappelli, Phys. Rev. E **63**, 026410 (2001).
[20] N. Z. Warner, J. J. Szabo, and M. Martinez-Sanchez, in *Proceedings, 28th International Electric Propulsion Conference*, Toulouse, 2003 (Electric Rocket Propulsion Society, Cleveland, OH, 2003), IEPC Paper 2003-082.
[21] E. Ahedo, P. Martinez-Cerezo, and M. Martinez-Sanchez, Phys. Plasmas **8**, 3058 (2001).
[22] A. Fruchtman, N. J. Fisch, and Y. Raitses, Phys. Plasmas **8**, 1048 (2001); see also: A. Cohen–Zur, A. Fruchtman, J. Ashkenazy, and A. Gany, Phys. Plasmas **9**, 4363 (2002).
[23] M. Keidar, I. Boyd, and I. Beilis, in *Proceedings, 38th Joint Propulsion Conference and Exhibit*, Indianapolis, 2002 (American Institute of Aeronautics and Astronautics, Reston, VA, 2002), AIAA Paper 2002-4107.
[24] L. Dorf, V. Semenov, Y. Raitses, and N. J. Fisch, in *Proceedings, 38th Joint Propulsion Conference and Exhibit*, Indianapolis, 2002 (American Institute of Aeronautics and Astronautics, Reston, VA, 2002), AIAA Paper 2002-4246.
[25] F. Taccogna, S. Longo, and M. Capitelli, Phys. Plasmas **12**, 093506 (2005).
[26] L. Dorf, Y. Raitses, V. Semenov, and N. J. Fisch, Appl. Phys. Lett. **84**, 1070 (2004).
[27] L. Dorf, Y. Raitses, and N. J. Fisch, J. Appl. Phys. **97**, 103309 (2005). See also: L. Dorf, Ph.D. Dissertation, Princeton University, Princeton, NJ, 2004.
[28] L. Dorf, Y. Raitses, and N. J. Fisch, Rev. Sci. Instrum. **75**, 1255 (2004).
[29] L. Dorf, V. Semenov, and Y. Raitses, Appl. Phys. Lett. **83**, 2551 (2003).
[30] J. E. Foster and A. D. Gallimore, Phys. Plasmas **3**, 4239 (1996).
[31] N. A. Kervalishvili, V. P. Kortkhondzhiya, and G. B. Machabeli, Sov. Phys. Tech. Phys. **20**, 512 (1975).
[32] E. V. Shun'ko, Phys. Lett. A **128**, 433 (1988).
[33] L. Pekker, Plasma Sources Sci. Technol. **4**, 31 (1995).
[34] M. A. Hassouba, Eur. Phys. J. A **14**, 131 (2001).
[35] K. Wasa and S. Hayakawa, *Handbook of Sputter Deposition Technology: Principles, Technology, and Applications* (Noyes, Park Ridge, NJ, 1992).
[36] A. Kovalenko and Yu. Kovalenko, Tech. Phys. **48**, 1413 (2003).
[37] Yu. Popov and Yu. Zolotaikin, Sov. J. Plasma Phys. **3**, 210 (1977).
[38] Yu. Popov, Sov. Phys. Tech. Phys. **15**, 1311 (1971).
[39] Y. Raitses, D. Staack, A. Smirnov, and N. J. Fisch, Phys. Plasmas **12**, 073507 (2005); see also: Y. Raitses, D. Staack, L. Dorf, and N. J. Fisch, in Proceedings, 39th Joint Propulsion Conference and Exhibit, Huntsville, 2003 (American Institute of Aeronautics and Astronautics, Reston, VA, 2003), AIAA Paper 2003-5153.
[40] Y. M. Kagan and V. I. Perel, Sov. Phys. Tech. Phys. **13**, 1348 (1969).
[41] A. Smirnov, Y. Raitses, and N. J. Fisch, Phys. Plasmas **11**, 4922 (2004).
[42] M. Keidar, I. D. Boyd, and I. I. Beilis, Phys. Plasmas **8**, 5315 (2001).
[43] A. Smirnov, Y. Raitses, and N. J. Fisch, J. Appl. Phys. **92**, 5673 (2002).
[44] L. Garrigues, G. J. M. Hagelaar, J. Bareilles, C. Boniface, and J. P. Boeuf, Phys. Plasmas **10**, 4886 (2003).
[45] M. Touzeau, M. Prioul, S. Roche *et al.*, Plasma Phys. Controlled Fusion **42**, B323 (2000).
[46] A. I. Morozov, A. I. Bugrova, A. V. Desyatskov, Yu. A. Ermakov, M. V. Kozintseva, A. S. Lipatov, A. A. Pushkin, V. K. Khartchevnikov, and D. V. Churbanov, Plasma Phys. Rep. **23**, 587 (1997).
[47] V. S. Golubev, Yu. N. Krivenko, P. G. Leonov, and V. B. Flerov, Sov. Tech. Phys. Lett. **14**, 662 (1988).
[48] A. I. Bugrova, L. M. Volkova, V. A. Ermolenko, E. A. Kral'kina, A. M. Devyatov, and V. K. Kharchevnikov, High Temp. **19**, 822 (1981).
[49] V. Yu. Fedotov, A. A. Ivanov, G. Guerrini, A. N. Vesselovzorov, and M. Bacal, Phys. Plasmas **6**, 4360 (1999).
[50] G. J. M. Hagelaar, J. Bareilles, L. Carrigues, and J.-P. Boeuf, J. Appl. Phys. **93**, 67 (2003).
[51] R. R. Hofer, Ph.D. dissertation. University of Michigan, Ann Arbor, MI 2004.